

## AIR-MRF: Accelerated iterative reconstruction for magnetic resonance fingerprinting

Christopher C. Cline <sup>a,b,1</sup>, Xiao Chen <sup>a,\*<sup>1</sup></sup>, Boris Mailhe <sup>a</sup>, Qiu Wang <sup>a</sup>, Josef Pfeuffer <sup>c</sup>, Mathias Nittka <sup>c</sup>, Mark A. Griswold <sup>d</sup>, Peter Speier <sup>c</sup>, Mariappan S. Nadar <sup>a</sup>

<sup>a</sup> Medical Imaging Technologies, Siemens Medical Solutions USA, Inc., Princeton, NJ, USA

<sup>b</sup> Department of Biomedical Engineering, University of Minnesota, Minneapolis, MN, USA

<sup>c</sup> Siemens Healthcare, Application Development, Erlangen, Germany

<sup>d</sup> Radiology, Case Western Reserve University, Cleveland, OH, USA



### ARTICLE INFO

#### Article history:

Received 23 November 2016

Received in revised form 10 July 2017

Accepted 10 July 2017

#### Keywords:

MRF  
Iterative  
Accelerated  
Compression  
Fast matching  
Regularization

### ABSTRACT

Existing approaches for reconstruction of multiparametric maps with magnetic resonance fingerprinting (MRF) are currently limited by their estimation accuracy and reconstruction time. We aimed to address these issues with a novel combination of iterative reconstruction, fingerprint compression, additional regularization, and accelerated dictionary search methods. The pipeline described here, accelerated iterative reconstruction for magnetic resonance fingerprinting (AIR-MRF), was evaluated with simulations as well as phantom and *in vivo* scans. We found that the AIR-MRF pipeline provided reduced parameter estimation errors compared to non-iterative and other iterative methods, particularly at shorter sequence lengths. Accelerated dictionary search methods incorporated into the iterative pipeline reduced the reconstruction time at little cost of quality.

© 2017 Elsevier Inc. All rights reserved.

## 1. Introduction

Magnetic Resonance Fingerprinting (MRF) is a recently proposed technique for quantitative MRI that has gained widespread attention for its novel approach and potential to rapidly image multiple tissue parameters simultaneously [1]. Multiparametric quantitative MRI has potential to provide notable improvements in clinical applications such as classification of tissue pathologies in cancer or other disease states [1–4]. However, current barriers to clinical adoption include potentially long acquisition and image reconstruction times required to achieve high quality parameter maps.

The originally proposed MRF method in [1] utilizes a pseudorandom pulse sequence to generate characteristic signal evolutions, the so-called fingerprints, indicative for different tissues distinguished by specific quantitative parameters such as the longitudinal relaxation time T1 and the transversal relaxation time T2. The measured response is then mapped to a precalculated dictionary of possible responses to reconstruct quantitative parameter maps. To capture the dynamics of the non-steady-state signal evolution, a single image is reconstructed for each TR, and thus the collected data for each image is highly undersampled and the reconstructed images contain a high level of aliasing artifacts. The original MRF reconstruction method treats these

aliasing artifacts as noise; a prolonged sequence length is thus used to provide enough data to robustly match the measured fingerprints to dictionary entries.

Iterative reconstruction methods have been proposed to improve reconstruction quality with promising results. In [5], the reconstruction is iterated between a gradient step and a mapping step. In [6,7], the signal evolutions are iteratively reconstructed first, and a final one-time mapping step is taken to produce the parameter maps. The increased image quality, however, comes at the cost of additional reconstruction time beyond the already time-intensive non-iterative reconstruction and the matching process.

Given a single voxel Bloch response  $X_i$ , the matching process searches the dictionary  $D$  for the atom with the highest correlation. In most MRF studies published so far, this matching is performed as an exhaustive inner product (EIP) between the measured signal and every atom in the dictionary. The complexity of this EIP search for an entire image scales proportionally to the number of atoms in the dictionary, the number of voxels in the image, and the number of TRs in the pulse sequence. To speed up reconstruction, two main categories of approaches have been explored: (1) reducing the effective size of the dictionary and (2) making dictionary matching more efficient. In [8], the dictionary is compressed using singular value decomposition (SVD). With reduced dimensionality along the temporal direction, matching time can be reduced by a factor of the compression rate. In [9], a low resolution dictionary is used for search acceleration and the reconstruction algorithm is designed to cope with the poor resolution by interpolating parameter

\* Corresponding author.

E-mail address: [xiao-chen@siemens.com](mailto:xiao-chen@siemens.com) (X. Chen).

<sup>1</sup> Equal contribution.

estimates in voxels that do not match existing dictionary atoms well. The other main approach is to accelerate dictionary search by replacing the exhaustive search through all atoms in a dictionary with a more efficient data structure and approximate search, such as in [10].

In this work, we propose an accelerated iterative reconstruction (AIR-MRF) pipeline that integrates dictionary compression, regularization, accelerated matching, and other techniques into a cohesive reconstruction method for faster and more accurate MRF reconstruction.

## 2. Materials and methods

### 2.1. Iterative MRF reconstruction

The complete AIR-MRF pipeline is depicted in Fig. 1. We adapted the iterative projection method proposed in [5], which applies compressed sensing theory to formulate the MRF problem as:

$$\min_{\hat{X}} \|Y - G(\hat{X})\|_2^2$$

$$\text{s.t. } \hat{X} = D(\hat{X})$$

where  $\hat{X}$  is the estimated image series and  $Y$  is the measured k-space data.  $G$  is an observation operator and  $G(X) = FSX$ , where  $S$  is the coil sensitivity map in the case of multi-channel acquisition,  $F$  is the Fourier transform, and  $M$  models undersampling. As implemented here, sampling is performed with a series of single-shot spiral trajectories in k-space, and  $M$  and  $F$  together are implemented with a non-uniform fast Fourier transform (NUFFT) [11].  $D(\hat{X})$  is the projection of  $\hat{X}$  into the dictionary. The problem can be solved by the Projected Landweber Algorithm (PLA) [12] as an extension of the iterative hard thresholding algorithm [13,14]. The estimated image series  $\hat{X}$  is iteratively updated from iteration  $(n)$  to  $(n+1)$  with

$$\hat{X}^{(n+1)} = D(\hat{X}^{(n)} + \alpha(G^H Y - G^H G \hat{X}^{(n)})) \quad (1)$$

where  $\alpha$  is a step size. Convergence is quantified by examining values of the cost function term  $\|Y - G\hat{X}^{(n)}\|_2^2$ , which is the data fidelity error.

#### 2.1.1. Iterative MRF with fingerprint compression

As proposed in [8], the fingerprints can be compressed through SVD along the temporal dimension after image reconstruction, to save time in the dictionary projection step. In this study, we modified the iterative reconstruction algorithm to operate directly in a compressed space and perform the compression before the image reconstruction to further reduce the reconstruction time.

Specifically, the new iterative update equation is given by

$$\hat{X}_c^{(n+1)} = D_c(\hat{X}_c^{(n)} + \alpha(G_c^H Y - G_c^H G_c \hat{X}_c^{(n)})) \quad (2)$$

The subscript  $c$  represents the compressed domain.  $X_c = CX$  where  $C$  is a compression operator that is obtained through an SVD of the dictionary, truncated to keep a reduced set of significant basis functions, and applied as a matrix multiplication [8]. Note that the dictionary projection operator  $D_c$  operates in the compressed SVD space. The  $G_c$  is an observation operator with integrated compression and defined as

$$G_c(X_c) = MFSC^H X_c = MC^H FSX_c$$

Note that the latter form is arranged such that the Fourier transform is applied to compressed signals, thus leading to fewer Fourier transform operations and reduced reconstruction time at each iteration. Additional advantages of this method of compression when applied to non-Cartesian, highly undersampled data will be discussed in Section 4.1.

With the matching of the signal from the  $i^{\text{th}}$  voxel to the  $\hat{k}^{\text{th}}$  atom in the dictionary described by

$$\hat{k}_i = \arg \max_k \frac{|\langle D_{ck}, \hat{X}_{ci} \rangle|}{\|D_{ck}\|_2} \quad (3)$$

the proton density is estimated as

$$\hat{\rho} = \frac{\langle D_{c\hat{k}_i}, \hat{X}_{ci} \rangle}{\|D_{c\hat{k}_i}\|_2 \|D_{k_i}\|_2} \quad (4)$$

Analogous equations are also used for matching in the uncompressed case. In both the uncompressed and compressed cases, the complex-valued estimated fingerprint is phase-corrected prior to matching to align its phase with the dictionary atoms. The phases of the fingerprint and the dictionary atoms are assumed constant along time. In the uncompressed case, the phases are estimated from the temporally-averaged signal. In the compressed case, the phases are estimated from the first principle component. The acquired signals are then phase compensated by the difference between the fingerprint and the dictionary.

### 2.2. Convergence of iterative reconstruction

Convergence behavior is critical to iterative reconstruction methods. Step size selection and regularization have direct impacts on the number of iterations needed for reconstruction and therefore overall reconstruction time, as well as the accuracy of the resulting parameter estimates.

#### 2.2.1. Adaptive step size selection

Convergence and reconstruction performance depend on selection of a suitable step size,  $\alpha$ , in each iteration. The  $\alpha$  is initialized as equal to the

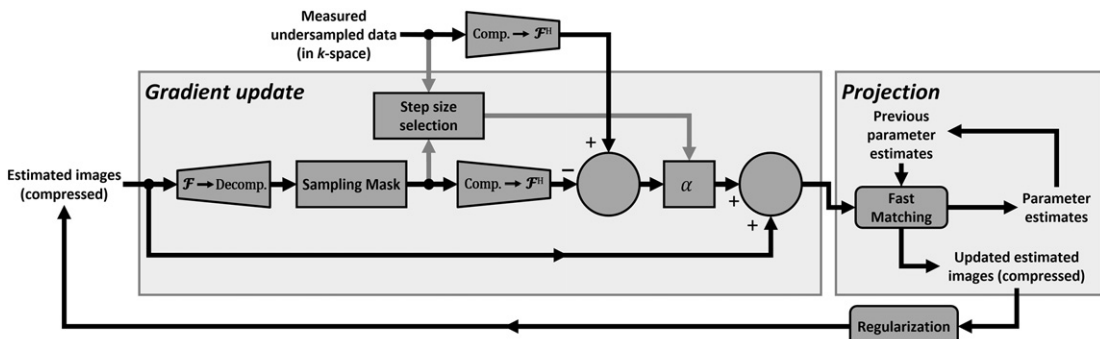


**Fig. 1.** Block diagram of the accelerative iterative reconstruction for magnetic resonance fingerprinting (AIR-MRF) pipeline.

undersampling rate. After the first iteration, a warm-start scaling factor,  $\beta$ , is calculated from the ratio of the energy of the current estimation over that of the acquired data.

$$\beta = \frac{\|G_c \hat{X}_c^{(1)}\|_2^2}{\|Y\|_2^2}$$

This  $\beta$  factor is applied to scale both  $\alpha$  and the first estimation for the next iteration. For each iteration after the first iteration, we calculate a candidate update for  $\hat{X}_c$  according to Eq. (2). If either

$$\alpha \leq 0.99 \frac{\|\hat{X}_c^{(n+1)} - \hat{X}_c^{(n)}\|_2^2}{\|G_c^H G_c (\hat{X}_c^{(n+1)} - \hat{X}_c^{(n)})\|_2^2} \quad (5)$$

or

$$\|G_c^H Y - G_c^H G_c \hat{X}_c^{(n+1)}\|_2^2 \geq \|G_c^H Y - G_c^H G_c \hat{X}_c^{(n)}\|_2^2 \quad (6)$$

is false, then the candidate update is rejected, the step size is halved, and a new candidate update is calculated. This continues until a candidate passes both conditions. Eq. (5) is based on the iterative hard thresholding algorithm as described in [5,15], and helps to improve the convergence behavior of the reconstruction algorithm.

### 2.2.2. Additional regularization

The spiral k-space sampling trajectories used here do not sample at the high spatial-frequency corners of k-space; as a result, the iteratively reconstructed images can be prone to high spatial-frequency artifacts. An example of these artifacts is shown in Fig. 2. Fig. 2A shows the image of the first principal component after compression at the 10th iteration, and Fig. 2B shows the corresponding k-space representation of the image in Fig. 2A. Energies from the central spiral-covered region and the peripheral region of k-space of the first principal component calculated at each iteration are shown in Fig. 2C. The energies after the gradient update step and after the dictionary matching step are plotted separately. The peripheral energy accumulates in each iteration even after the center region has converged. Most of the increase in the energy

of the peripheral k-space region occurs in the matching step of each iteration.

Those high frequencies arise because the Bloch manifold used as a regularizer is a cone (i.e. it is stable to linear scaling of the proton density), therefore it is not bounded. This is different from the spatial regularizations often encountered in imaging such as Tikhonov or wavelet L1-norm, which constrain the image to a bounded set and guarantee stable reconstructions irrespective of the sampling method. The MRF regularized reconstruction problem as a whole can still be well-posed if there is no non-zero intersection between the null space of the measurement operator and the admissible directions of the Bloch constraint at any solution. However, the divergence of high frequencies shows that this is not the case with spiral sampling: there are admissible image distortions whose k-space supports lie entirely in the unsampled k-space corners, and Bloch regularization seems to be compatible with k-space interpolation (i.e. a compressed sensing task) but not k-space extrapolation (i.e. a super-resolution task.)

To address this issue, we apply spatial regularization to the PD map. Specifically, a low-pass filter with a radius determined solely by the acquired spiral trajectories is applied to the spectrum of the estimated PD map. The low-pass filtered PD is then used to scale the matched fingerprint to generate the image estimates for the next iteration. The circular low-pass filter is defined by two concentric circles in k-space, where the stop-band radius equals the maximum k-space trajectory and the pass-band radius equals 85% of the stop-band radius. The filter ramps linearly from 0 to 1 in the transient band to mitigate Gibbs ringing artifacts.

### 2.3. Accelerated search incorporating information from previous iteration

To accelerate the parameter estimation step, we structured the dictionary in a k-dimensional tree (kd-tree) and treated the matching problem as an approximate nearest neighbor (ANN) search, with the measured signal  $\hat{X}$  being a query point in a high dimensional feature space. In particular, we used a single randomized kd-tree algorithm as implemented in the Fast Library for Approximate Nearest Neighbors (FLANN) [16,17]. We construct the kd-tree once during the dictionary generation process, and then reuse the search structure quickly during each repetition of the image reconstruction.

During a typical kd-tree search, an initial candidate match is obtained by traversing the tree from root to a leaf node, deciding at each level of

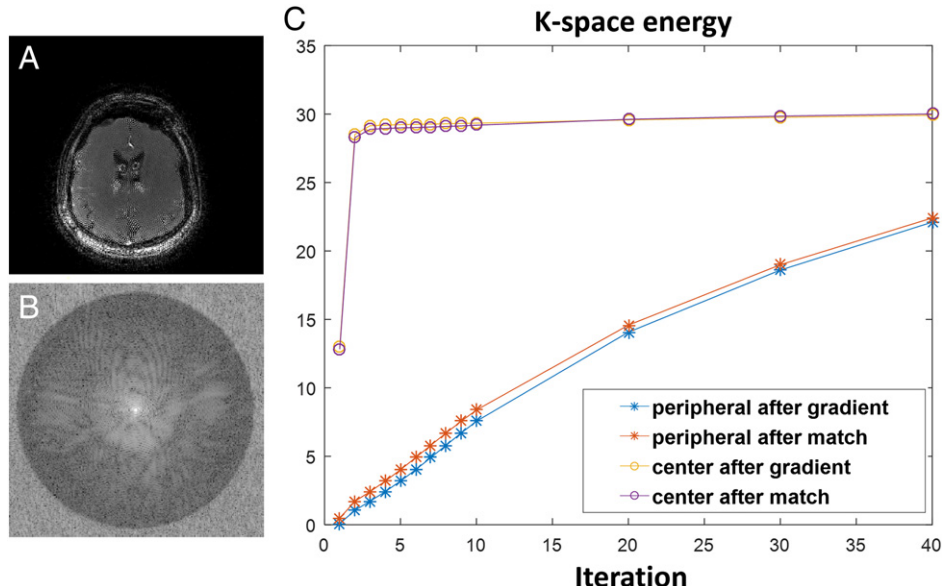


**Fig. 2.** Example of high-frequency artifacts resulting from unregularized iterative reconstruction. (A) reconstructed image of the first principal component of data series, (B) k-space representation of (A), and (C) plot of energy in two regions of k-space over the course of iterative reconstruction.

the tree which branch to follow by comparing a single dimension of the query point to the branch's position in the same dimension [17]. The distance between the initial candidate match and the query defines the radius of a hypersphere; any cell of the kd-tree that intersects this hypersphere may contain a closer match than the initial candidate. Exhaustive search would require checking all possible matches within this hypersphere, which in some cases could involve searching every single leaf node in the tree. Approximate nearest-neighbor search obtains a reduction in search time here by only checking a fixed number of leaf nodes within this hypersphere. The best match after a limited number of leaf node checks is considered the approximate match to the query.

For MRF signal search, a complex-valued fingerprint that contains  $L$  time points or components is normalized and converted to a  $2L$ -length real-valued vector containing the separated real and the imaginary parts for use as a query. Each of the  $2L$  time points or components corresponds to one dimension in the kd-tree and thus during tree traversals at each node of the tree the query fingerprint is compared with a dictionary entry at a single dimension. The similarity between the query fingerprint and a given dictionary match is quantified using Euclidean distance in this  $2L$ -dimensional space. With suitable normalization of the fingerprints prior to calculating the  $2L$  Euclidean distance, minimization of distance is equivalent to maximization of similarity, since there is a monotonically decreasing relationship between the distance and similarity. This matching procedure replaces Eq. (3) during accelerated reconstruction; Eq. (4) is still used to estimate the proton density.

During iterative MRF reconstruction, we can assume that the parameter estimates for a given voxel will not typically change drastically from one iteration to the next. To take advantage of this, we modified the kd-tree implementation in FLANN to further reduce search times. For every iteration after the first, we take the previous iteration's parameter estimate as an initial guess for the closest dictionary match to the new query, and immediately eliminate cells of the kd-tree that cannot contain closer matches. If a measured fingerprint does change drastically between iterations, the initial guess will in the worst case not eliminate any cells of the tree and the search will proceed as it normally does with no prior information. By incorporating this prior information, we can obtain acceleration beyond what would be obtained with conventional kd-tree search alone.

The AIR-MRF reconstruction algorithm combines both compression and approximate search into the iterative framework. In this case, the kd-tree is constructed from the compressed dictionary and each dimension in the high-dimensional search space is a single SVD component rather than a single TR measurement.

## 2.4. Experiments

### 2.4.1. Sequence

A prototype unbalanced SSFP pulse sequence with an initial inversion pulse followed by a train of pseudorandom flip angles (FAs, 0–75°) and repetition times (TRs, 12–15 ms) was used [18]. A dual-density spiral trajectory was designed with 48 interleaves [19], inner/outer density (2,1) transitioning at a relative radius of 0.45. The spiral readout duration was 5.0 ms sampled with 2.5 μs dwell time and TE of 3.7 ms. At each TR k-space data was collected on one of the 48 spiral interleaves. The single-shot spiral interleaf was uniformly rotated by 7.5° with each TR. A sequence length of 3000 TRs was used. Acquisitions at shorter sequence lengths were retrospectively generated by discarding data from the end of the sequence. The constructed dictionary consisted of 5366 atoms with T1 ranging from 10 to 4500 ms (increments of 10, 20, 40, and 100 for ranges 10 to 100, 120 to 1000, 1040 to 2000, and 2050 to 4500, respectively, in ms) and T2 ranging from 2 to 3000 ms (increments of 2, 5, 10, 50, 100, and 200 for ranges 2 to 10, 15 to 100, 110 to 300, 350 to 800, 900 to 1600, and 1800 to 3000, respectively, in ms), excluding combinations of T1 and T2 values where T1 < T2. AIR-MRF results presented below used compressed fingerprints truncated to 150

components for the pulse sequence length of 3000 TRs, and to 300 components for the longer sequence lengths.

### 2.4.2. Digital phantom

Ground truth T1, T2, and PD values were obtained from one slice of the BrainWeb digital phantom [20] at a field strength of 1.5 T, zero padded to be square. The 434 × 434 image was nearest-neighbor downsampled to 256 × 256. Bloch responses for both dictionary generation and generation of simulated data were calculated from ground truth values using Bloch simulations. Data both with and without noise were used for reconstructions.

To generate the data with noise, complex white noise was added to the k-space simulated brain synthetic data with a mean peak signal-to-noise ratio of 60. Each experiment for a specific reconstruction method and sequence length was repeated 10 times with different noise instances. Statistical significance was assessed with unpaired Student's t-tests. The acquisition was simulated as a single channel acquisition.

### 2.4.3. Phantom and *in vivo* data

The NIST referenced quantitative MRF phantom [21] has been used previously to assess MRF reconstruction quality [22]. In this study, a NIST phantom was scanned using the above mentioned sequence on a MAGNETOM Aera 1.5 T MR scanner (Siemens Healthcare, Erlangen, Germany) with the following parameters: FOV 300 × 300 mm<sup>2</sup>, resolution 1.17 × 1.17 mm<sup>2</sup>, slice thickness 5 mm. Volunteer data were acquired using the same sequence and system after informed consent was obtained. A 20-channel head coil was used. Coil sensitivity maps were calculated following the method in [23] using the k-space central region (12 × 12) after gridding the temporal averaged MRF data.

### 2.4.4. Assessment

Parameter estimation errors were quantified for a parameter  $\theta \in \{T1, T2, PD\}$  using

$$\text{error}_\theta = \frac{1}{N} \sum_i^N \frac{|\theta_i - \hat{\theta}_i|}{\theta_i}$$

where  $\theta$  and  $\hat{\theta}$  represent the reference and estimated parameter values, respectively.  $N$  is the number of pixels within a mask over the support of the object of interest. For the synthetic phantom, the object mask was obtained by combining the white matter, grey matter, and cerebrospinal fluid masks. For the NIST phantom, the object mask included 14 automatically contoured regions over the small tubes and 2 manually contoured regions from the main phantom. For the *in vivo* data, the object mask was obtained by manually contouring the estimated PD map of the whole brain.

In this study, we compared AIR-MRF to non-iterative reconstruction (NIR-MRF) and iterative reconstruction (IR-MRF) without dictionary compression and proton density regularization.

## 3. Results

**Fig. 3** shows AIR-MRF reconstruction results from the synthetic data for a range of pulse sequence lengths and compression amounts, along with the ground truth (A–C). Excellent qualities of T1 and proton density maps were achieved by AIR-MRF, even with sequence lengths shortened from 3000 (D–F) to 1200 (G–I) and 300 (J–L) TRs. The T2 map at a length of 1200 TRs (H) closely resembles the ground truth. Some artifacts are visible on the T2 map produced from a sequence length of 300 TRs (K).

Reconstruction performance with the simulated BrainWeb digital phantom for NIR-MRF, IR-MRF, and AIR-MRF are compared in **Figs. 4 and 5**. **Fig. 4** shows the reconstructed T2 maps. High quality estimation was consistently achieved using AIR-MRF (G–I) at different sequence lengths. Aliasing artifacts are visible on the NIR-MRF (A–C) and IR-MRF (D–F) results with the shorter sequence lengths, and severe aliasing

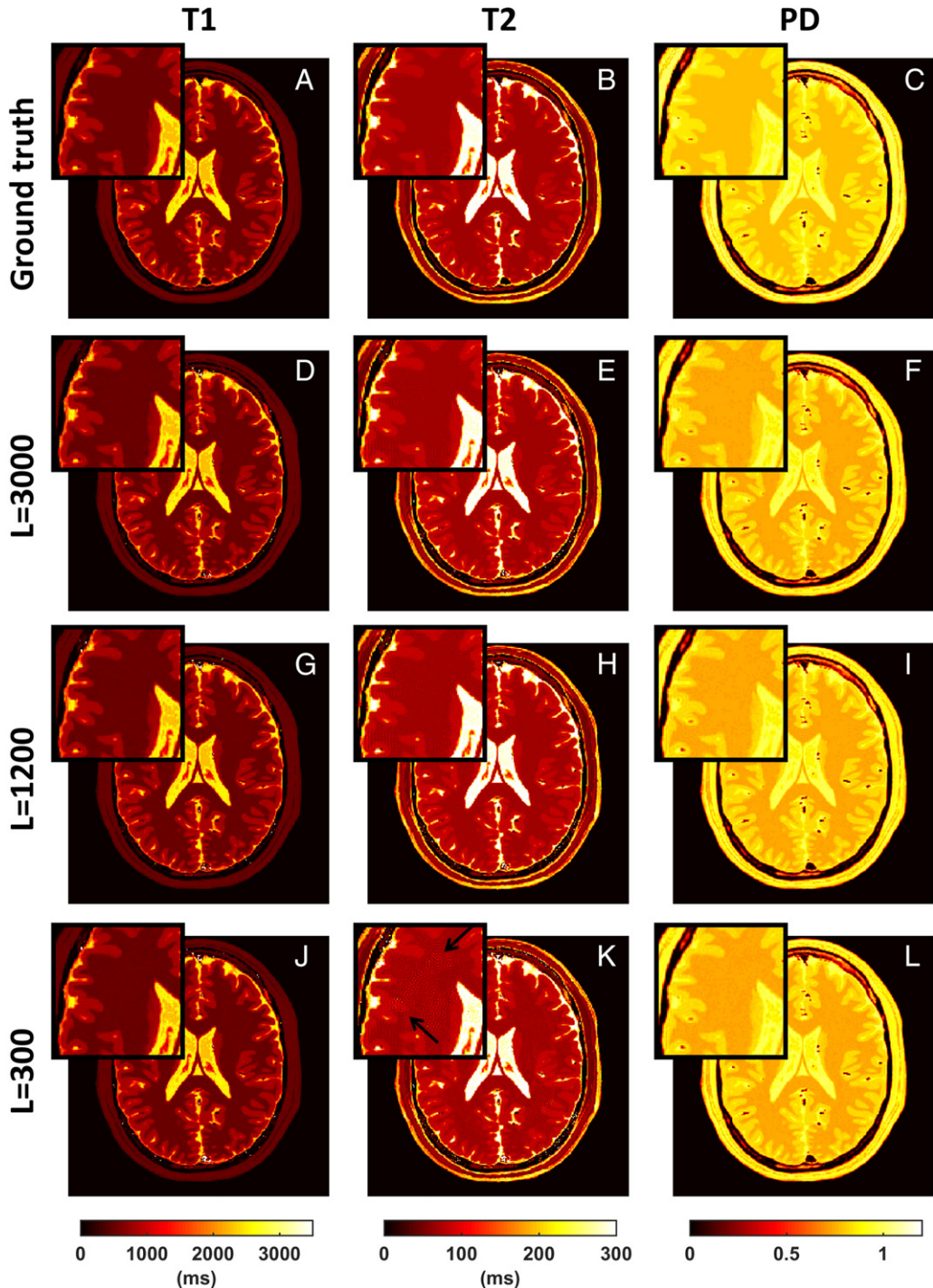


**Fig. 3.** Ground truth parameters from BrainWeb digital phantom and simulated AIR-MRF reconstruction results for a pulse sequence of 3000 compressed to 300 components, 1200 compressed to 300 components, and 300 compressed to 150 components.

artifacts occur at the shortest sequence length of 300. Quantitative analyses of T1, T2, and PD maps reconstructed by the three methods are shown in Fig. 5. AIR-MRF shows superior quality at all sequence lengths. The quality degradation due to the decreased amount of data is also minimal with AIR-MRF. The T2 estimation error curves agree with the artifact levels visible in Fig. 4.

Quantitative analyses of the synthetic BrainWeb digital phantom with added noise are summarized in Table 1. Mean error percentages are reported. AIR-MRF achieved significantly better T1 and PD estimations than IR-MRF and NIR-MRF at all sequence lengths. AIR-MRF achieved significantly better T2 estimation than IR-MRF and NIR-MRF

at a sequence length of 300 TRs, but slightly lower quality compared to IR-MRF at longer sequence lengths without significant differences. All the parameter estimations from IR-MRF and AIR-MRF had significantly lower errors comparing to NIR-MRF ( $p < 0.01$ ).

Fig. 6 compares the digital phantom reconstruction results produced by AIR-MRF using exhaustive search, AIR-MRF using approximate nearest neighbor search, and NIR-MRF using exhaustive search at various sequence lengths. AIR-MRF (ANN) provides similar quality as AIR-MRF (EIP) and both provide consistent improvements over NIR-MRF. The convergence behavior of AIR-MRF is demonstrated in Fig. 7, using the digital phantom data. Good convergence is achieved by both IR-MRF

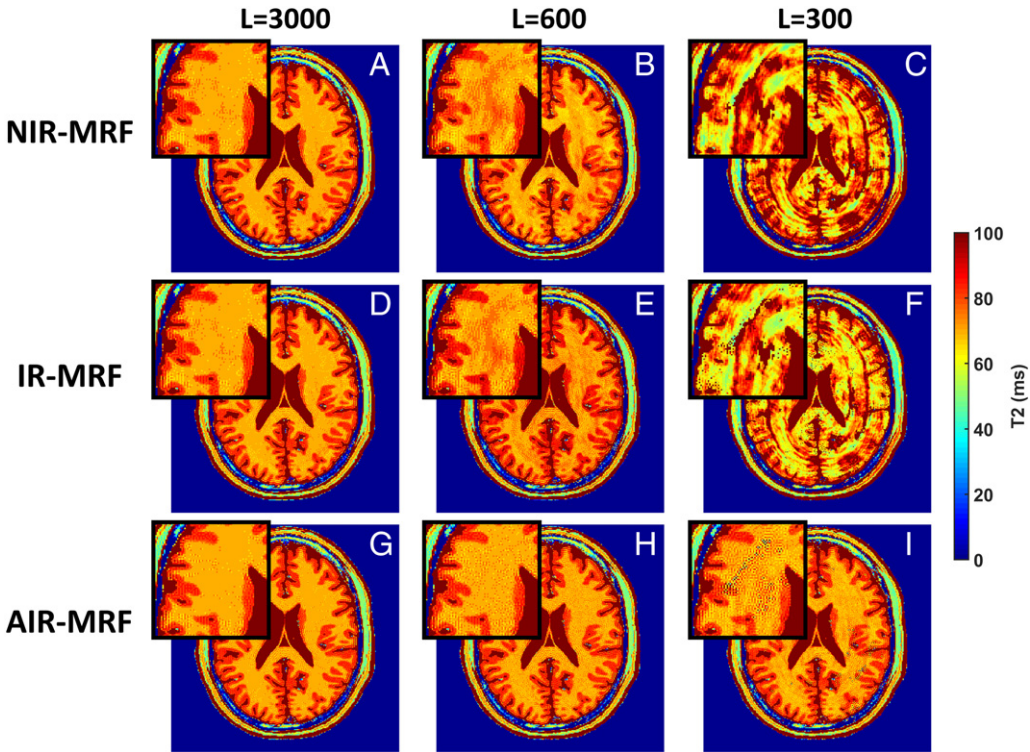


**Fig. 4.** T2 reconstruction results for NIR-MRF, IR-MRF, and AIR-MRF methods for pulse sequences with lengths of 3000, 600, and 300 TRs.

and AIR-MRF. However, the data fidelity error curve of AIR-MRF that incorporates compression reaches a lower minimum, indicating that the reconstruction more closely matches the observed measurements. With compression, the minimum value is also reached after fewer iterations than without compression.

Reconstruction performance with the scanned NIST phantom for NIR-MRF, IR-MRF, and AIR-MRF are compared in Figs. 8 and 9. T1, T2, and PD estimates are shown as reconstructed by the three methods at sequence length of 3000 TRs (Fig. 8A–I) and a shorter sequence of 600 TRs (Fig. 8J–R). Severe degradations in estimate accuracy of T2 for NIR-MRF (Fig. 8K) and IR-MRF (Fig. 8N) can be observed at the shorter sequence length. AIR-MRF is able to produce good results for T1, T2, and PD even at the shorter sequence length.

Fig. 9 shows a Bland-Altman analysis (Fig. 9A) and mean error percentage (Fig. 9B) for reconstruction results of various compartments of the NIST phantom. Results of NIR-MRF, IR-MRF, and AIR-MRF at sequence lengths of 2400, 1600, and 600 TRs are compared to the results using the corresponding method at a sequence length of 3000 TRs. For the two shorter pulse sequence lengths (600 and 1600 TRs), AIR-MRF outperformed the other two reconstruction methods tested, especially for the T2 estimation.

Fig. 10 shows the reconstruction performance for volunteer brain data for NIR-MRF, IR-MRF, and AIR-MRF. T1, T2, and PD estimates are

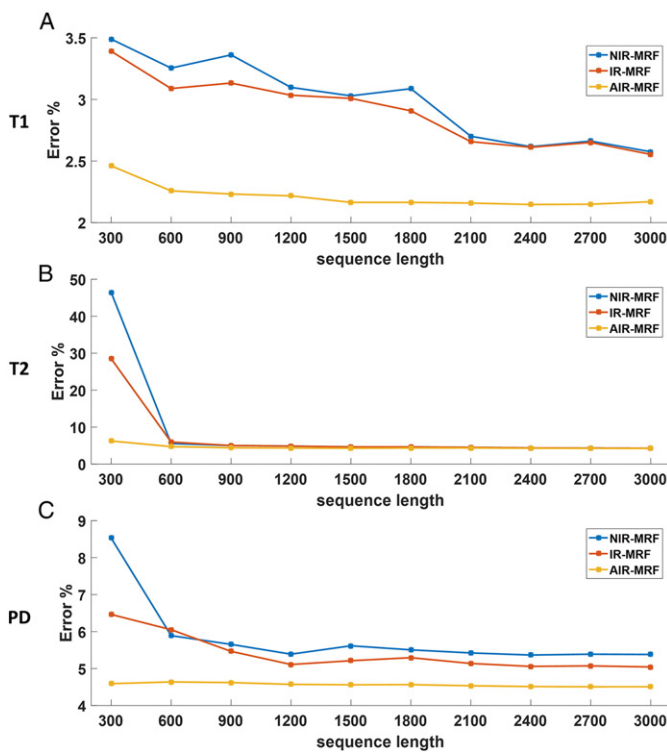


**Fig. 5.** Plots of quantitative results for the same simulated reconstructions as in Fig. 4.

**Table 1**

Quantitative analyses of the synthetic BrainWeb data with added noise. The reconstructed maps were compared to the ground truth maps and mean error percentages were calculated. Average values and standard deviations over 10 repetitions are shown. Statistical significance was assessed with unpaired Student's *t*-tests. \* indicates  $p < 0.01$  vs. AIR-MRF.  $p < 0.01$  vs. NIR-MRF for all IR-MRF and AIR-MRF results (not shown).

Parameter	Method	Sequence length		
		3000	1200	300
T1	NIR-MRF	$3.7 \pm 0.02^*$	$4.24 \pm 0.02^*$	$4.77 \pm 0.02^*$
	IR-MRF	$3.41 \pm 0.02^*$	$3.71 \pm 0.02^*$	$4.14 \pm 0.01^*$
	AIR-MRF	$3.35 \pm 0.01$	$3.65 \pm 0.04$	$3.97 \pm 0.01$
	NIR-MRF	$5.17 \pm 0.02^*$	$6.4 \pm 0.02^*$	$51.72 \pm 0.3^*$
	IR-MRF	$4.96 \pm 0.02$	$5.95 \pm 0.02$	$14.07 \pm 0.08^*$
	AIR-MRF	$4.97 \pm 0.02$	$6.02 \pm 0.07$	$11.6 \pm 0.05$
T2	NIR-MRF	$4.82 \pm 0.00^*$	$5.1 \pm 0.01^*$	$9.77 \pm 0.02^*$
	IR-MRF	$4.57 \pm 0.01^*$	$4.77 \pm 0.01^*$	$5.66 \pm 0.01^*$
	AIR-MRF	$4.59 \pm 0.00$	$4.69 \pm 0.01$	$5.31 \pm 0.01$
PD	NIR-MRF	$4.97 \pm 0.02^*$	$5.1 \pm 0.01^*$	$9.77 \pm 0.02^*$
	IR-MRF	$4.57 \pm 0.01^*$	$4.77 \pm 0.01^*$	$5.66 \pm 0.01^*$
	AIR-MRF	$4.59 \pm 0.00$	$4.69 \pm 0.01$	$5.31 \pm 0.01$

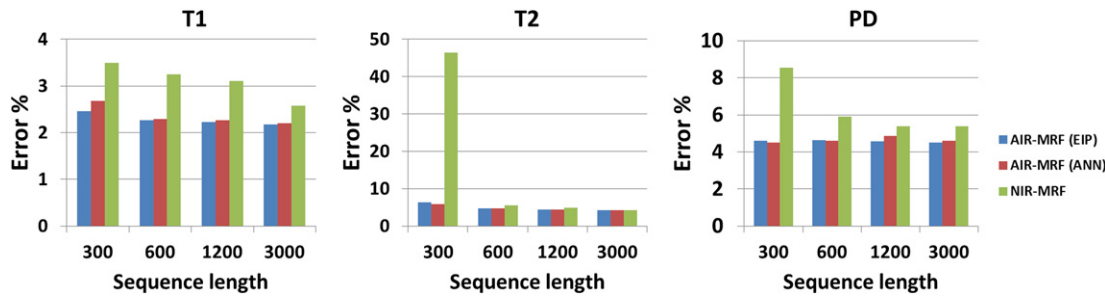


**Fig. 6.** Comparison of parameter estimate errors for the simulated phantom using AIR-MRF with exhaustive inner product (EIP) search, AIR-MRF with approximate nearest neighbor (ANN) search, and NIR-MRF.

shown as reconstructed by the three methods at a sequence length of 3000 TRs (A–I) and a shorter sequence of 300 TRs (J–R). At the longer sequence length, NIR-MRF and IR-MRF produced high quality tissue parameter maps. Some high spatial-frequency artifacts at tissue boundaries are visible on the results produced by IR-MRF. At the shorter sequence length, severe degradations of T2 maps reconstructed by NIR-MRF and IR-MRF can be observed. The results from AIR-MRF more closely resemble the results from the sequence length of 3000 TRs. Fig. 11 shows the mean error percentage for reconstruction results of the volunteer data. Results of NIR-MRF, IR-MRF, and AIR-MRF at sequence lengths of 2000, 1000, and 300 TRs are compared to the results using the corresponding method at a sequence length of 3000 TRs. AIR-MRF showed significant improvement over the other two methods at shorter sequence lengths.

Estimated parameter maps from acquired data reconstructed by AIR-MRF with and without proton density regularization are shown in Fig. 12. Without regularization, high spatial-frequency artifacts are apparent throughout the in vivo maps (G–I) and are mostly visible at the edge of the NIST phantom (A–C), as indicated by arrows. These artifacts are drastically reduced with proton density low-pass filter regularization (D–F, J–L).

Detailed reconstruction times including the time of the dictionary matching step per iteration, the time of the gradient step per iteration, the reconstruction time per iteration, and the total reconstruction time are summarized in Table 2. Synthetic Brainweb images with spatial size  $256 \times 256$  and sequence lengths of 3000 and 300 TRs were reconstructed by IR-MRF, AIR-MRF using exhaustive inner product, and AIR-MRF using ANN. The times were averaged over 10 repetitions and are shown in seconds in the table. Reconstructions were performed using MATLAB on a computer with a 32 core 2.4 GHz Intel Xeon CPU and 32 GB of RAM. FLANN parameters included: number of trees = 1 and number of leaves

to check = 256. AIR-MRF with ANN requires constructing the kd-tree structure once at the beginning of the reconstruction. This process takes about 5 s for the setup described here.

#### 4. Discussion

In this work, we have proposed an accelerated iterative reconstruction method for MRF. The iterative reconstruction was integrated with dictionary compression and fast matching methods that contribute to both increased parameter estimation quality and decreased reconstruction time. We have shown that AIR-MRF can allow for MRF scans at shorter sequence lengths that still offer high image quality, compared to other MRF reconstruction methods. Our previous work on iterative MRF [24] has been extended here to incorporate additional regularization and was tested on in vivo brain data.

##### 4.1. Effects of compression

A straightforward effect of dictionary compression along the time dimension is a decrease in reconstruction time. This is due to decreases in both the number of Fourier transform operations and the matching time. While performing an NUFFT on uncompressed data for a single image involves operating on a single highly undersampled spiral trajectory, performing an NUFFT on compressed data involves operating on an essentially fully-sampled set of k-space data. With compression, fewer NUFFT operations are required due to there being fewer compressed image components than uncompressed images. The time saved by performing fewer NUFFTs outweighs the increased time due to the increased amount of data for each NUFFT. By applying the NUFFT in the compressed signal space, the reduction in NUFFT operation time is almost proportional to the compression rate. The compression also leads to a time reduction in matching proportional to the compression rate when EIP matching is used, as reported in [8]. The combination of compression with the implemented approximate nearest-neighbor search method further decreases the reconstruction time at little cost of quality. In the AIR-MRF pipeline, the compression also leads to increased quality due to several interacting features of the method. The compression inherently exploits the low-rank property of the signal, which decreases the noise level in the images. We observed that “compressing” a measurement without truncating any SVD components (i.e. transforming a fingerprint into the SVD feature space without loss of information) resulted in better image quality and faster convergence speed than working with untransformed measurements (data not shown). Additionally, compression results in a “fully-sampled” dataset for each compressed image, making the density compensation function (DCF) estimation for the NUFFT more accurate. In terms of the approximate-nearest-neighbor kd-tree search, working with compressed signals allows construction of decision boundaries according to the less noisy principal components of fingerprints, rather than values at single time points. This improves search robustness in the presence of noisy measurements and allows higher search acceleration.

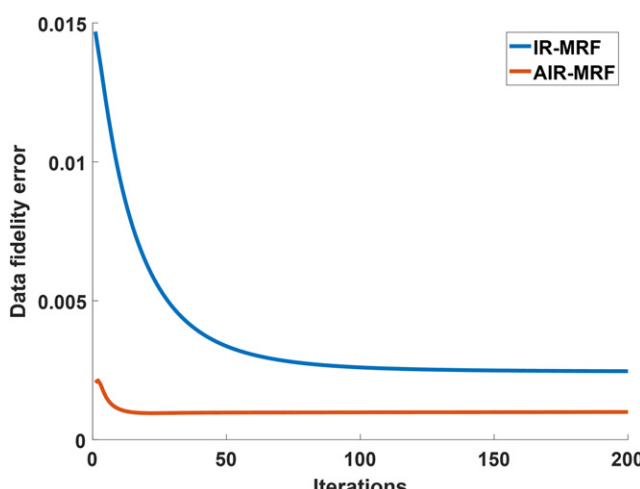


**Fig. 7.** Plot illustrating convergence behavior of IR-MRF and AIR-MRF.

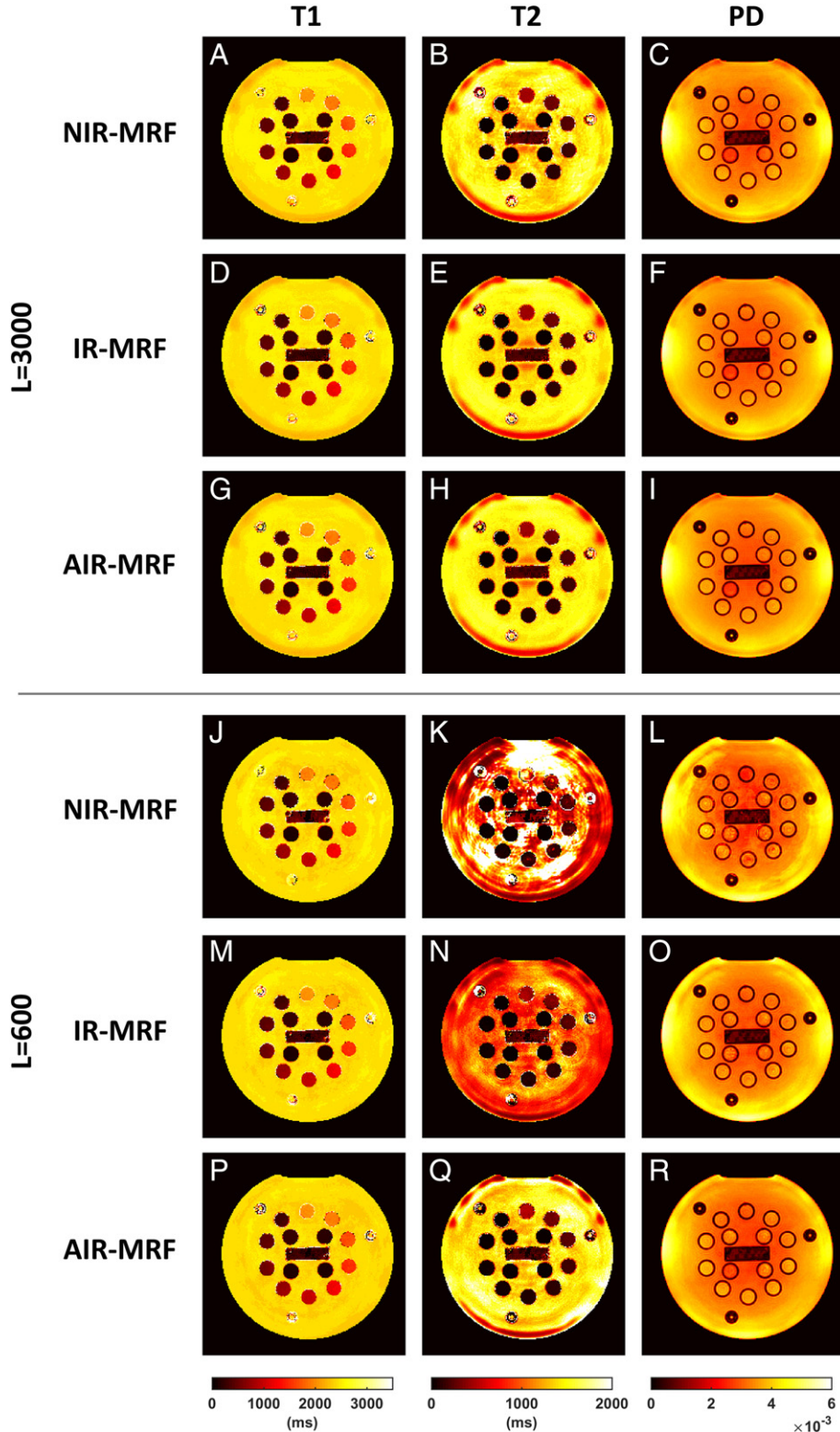


**Fig. 8.** NIST phantom reconstruction results for NIR-MRF, IR-MRF, and AIR-MRF methods, with a pulse sequence length of 3000 TRs (A–I) and 600 TRs (J–R).

In the current implementation, each entry in the vectors used for calculating similarity between the query signal and the dictionary atoms (in the uncompressed or compressed space) is evenly weighted. Studies have shown that a weighted metric can provide better correlation estimation [25]. This may be particularly beneficial to compressed reconstruction, since the energy distribution after compression is concentrated on the first few singular values or components.

#### 4.2. Convergence

With the utilization of the additional regularization term on proton density, high frequency artifacts that would otherwise dominate in later iterations are mostly suppressed. We have shown that the artifacts are introduced by the dictionary matching step, and that the gradient step that forces data fidelity cannot correct the introduced error in

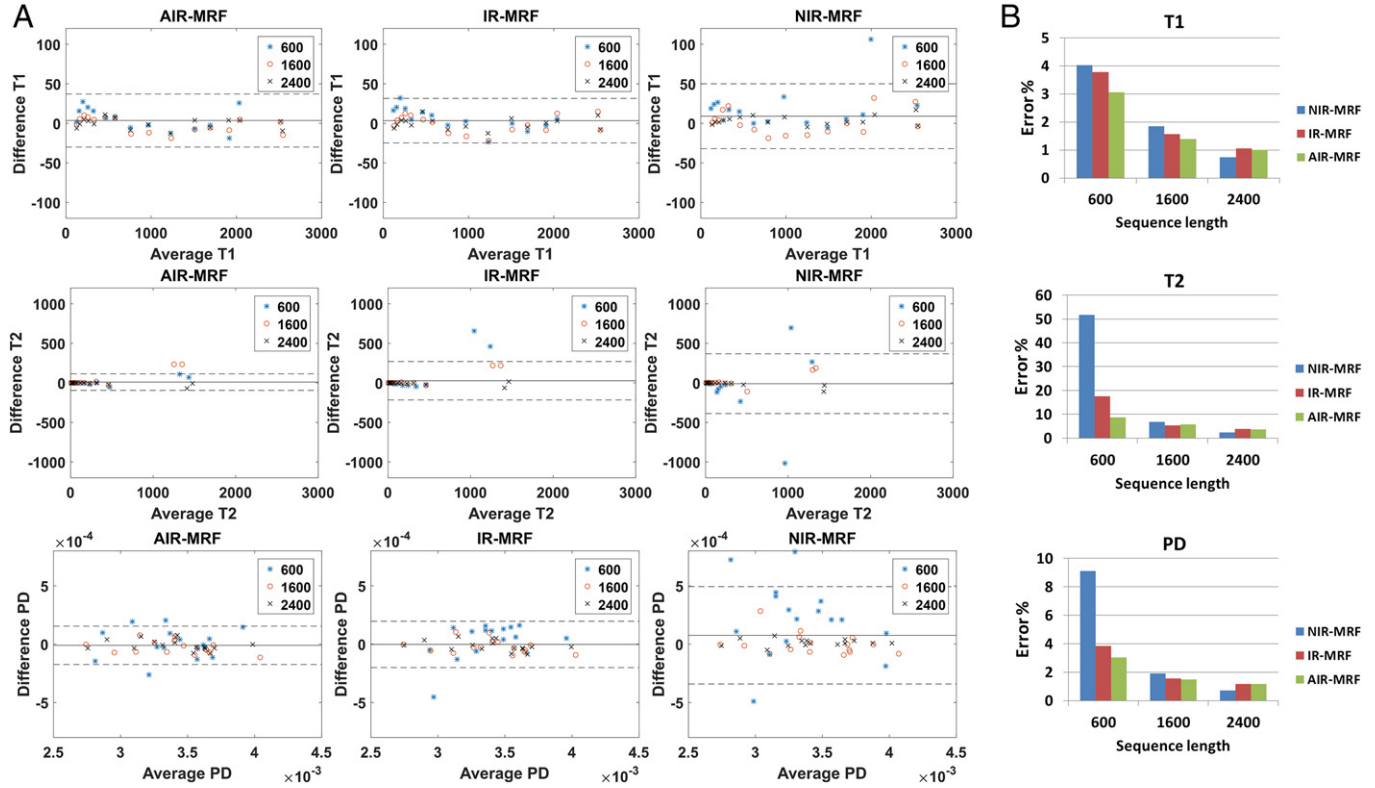


**Fig. 9.** Plots of quantitative results for reconstruction of NIST phantom scans for NIR-MRF, IR-MRF, and AIR-MRF for a range of sequence lengths. Bland-Altman plots (A) and mean relative errors (B) for reconstruction values vs. ground truth phantom values in specific ROIs. In (A), the solid line indicates mean difference and dashed lines indicate 95% limits of agreement in each subplot.

regions of k-space where data was not acquired. Correspondingly, the cost function cannot monitor the accumulation of these artifacts, and the reconstruction will be considered converged even if the artifacts become more prominent over additional iterations. Our current solution using a low-pass filter on the proton density map has been shown to be effective and efficient for removing these artifacts. It also indicates the necessity of additional regularization for iterative MRF reconstruction. We observed that without compression the artifacts became visible only after many iterations using our iterative framework, about 2500 iterations for synthetic data, 500 iterations for the NIST phantom, and about 25 iterations for the in vivo data. However, in the compressed reconstruction these artifacts become visible much earlier: as early as iteration 5 in our tests. Thus the regularization shows the most benefit when compression is used. Due to the role of the PD values in scaling the reconstructed Bloch responses, the energy in the high-frequency corners of k-space increases in the images and proton density map, but not on the T1 or T2 maps, so the LPF was only applied to the PD map. The additional computational time for this PD regularization is negligible in relation to overall reconstruction time. Regularization does not need to be constrained to parameter maps but can also be applied to the Bloch responses; such an approach has previously been shown beneficial to reconstruction quality [6]. In the future, we plan to explore additional regularization methods.

It is noteworthy on the NIST phantom results that signal non-uniformity can be observed at the edge of the phantom for all reconstruction methods. On GRE images and a B1 map that were separately acquired during the same scan, some non-uniformity regions could be found at the similar locations (results not shown). B1 map compensated MRF reconstruction methods have been proposed and shown to improve MRF reconstruction quality [3,26]. Future studies will incorporate more sophisticated MR signal models to include effects such as B1 inhomogeneity.

The update step size is initialized as the data undersampling rate and undergoes a warm-start initialization step for adjustment according to

the energy level after the first iteration. This has been shown to be effective in speeding up the rate of convergence. An adaptive step size adjustment mechanism is used for each iteration to ensure convergence of the cost function at the cost of additional repetitive iterations. In practice, we have observed that this step is rarely activated and that the step size is constant for iterations after the warm-start. All reconstructions conducted in this study exhibited favorable convergence behavior. At long sequence lengths of around 3000 TRs, only 1 to 2 iterations were needed. At shorter sequence lengths, such as 600 TRs, the cost function converged in around 5 to 10 iterations. The difference in ultimate image fidelity in the reconstructions shown in Fig. 7 and described in the results could be attributed to several factors. Both iterative reconstruction methods are not guaranteed to find global optima; even different instances of the same algorithm with different initializations may generate different solutions by converging to different local optima. The simulation results with multiple noise instances demonstrate that the apparent benefits of AIR-MRF are not due to convergence to a better local optima only in this particular case. The additional regularization, and the abilities of the compression to exploit low-rank properties of the signal and to handle density compensation during the NUFFT in a more accurate fashion could all contribute to the ultimate difference in fidelity.

In the current study, we have compared AIR-MRF to the iterative MRF method proposed in [5], to assess the effects of the compression and regularization components of AIR-MRF. In the future, we plan to conduct a rigorous comparison of the proposed AIR-MRF to other iterative methods [5,6,27,28].

#### 4.3. Sequence lengths

In this work, we have shown that by using AIR-MRF, the required sequence length to achieve an accurate estimate of tissue parameters can be decreased significantly. These shorter acquisition times will help to bring MRF techniques closer to clinical practice. Under the current

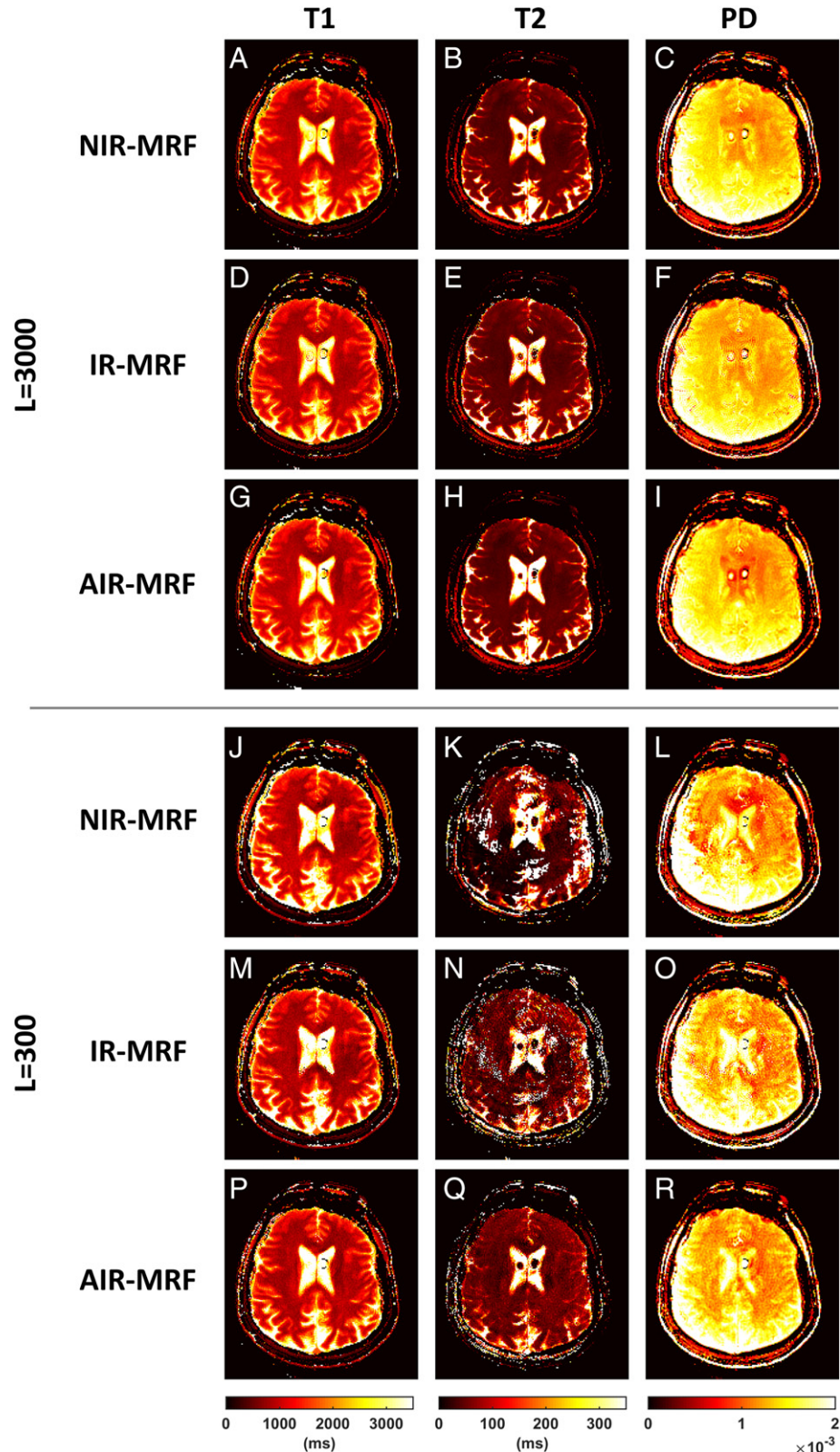


**Fig. 10.** In vivo reconstruction results for NIR-MRF, IR-MRF, and AIR-MRF with a pulse sequence length of 3000 TRs (A–I) and 300 TRs (J–R).

sequence design, the sequence length can be shortened from 3000 to 600 TRs by using AIR-MRF, without redesigning the encoding sequence. This measurement acceleration could not be achieved by using an existing non-iterative method with an otherwise similar setup without sacrificing reconstruction accuracy. Likewise, a similar iterative method without compression and regularization produced parameter estimates with

noticeable residual aliasing artifacts at shorter sequence lengths. At longer sequence lengths (e.g. 3000 TRs) we showed that reconstruction accuracies are comparable across the methods tested; with the assumption that the aliasing artifacts can be treated as noise, longer sequence lengths and compression effectively increase the SNR during dictionary matching, resulting in improved reconstruction results. In this study,

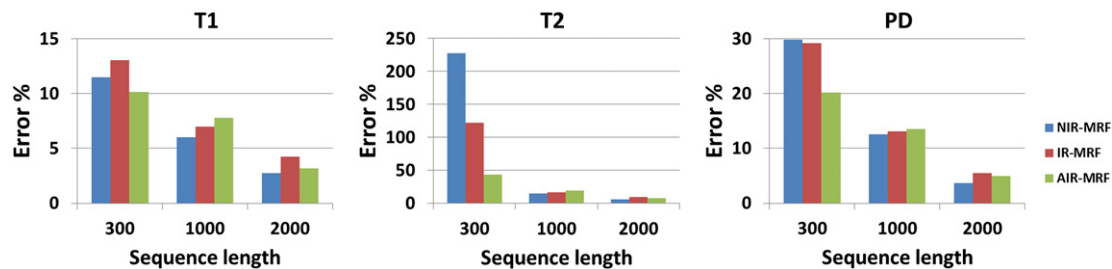


**Fig. 11.** Plots of mean error percentage for reconstruction of *in vivo* volunteer scans for NIR-MRF, IR-MRF, and AIR-MRF for a range of sequence lengths.

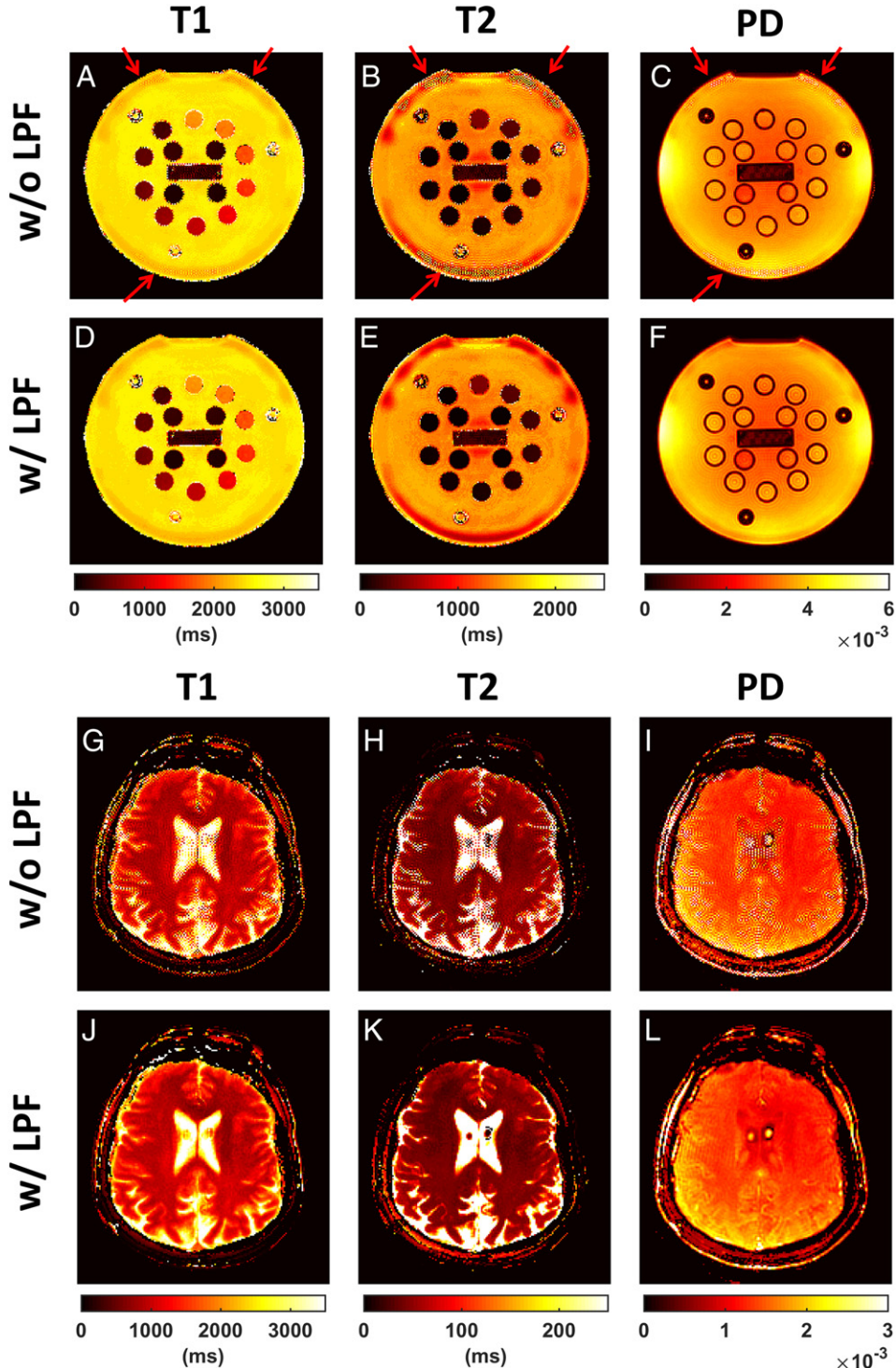


**Fig. 12.** AIR-MRF reconstruction results for phantom and *in vivo*, without (A–C, G–I) and with (D–F, J–L) proton density low-pass filter regularization.

**Table 2**

Reconstruction times of IR-MRF, AIR-MRF with EIP, and AIR-MRF with ANN. Synthetic Brainweb images with spatial size  $256 \times 256$  and sequence lengths of 3000 and 300 TRs were reconstructed. Times are shown in seconds.

Sequence lengths	Methods	Matching step (per iteration)	Gradient step (per iteration)	Time (per iteration)	Total time (10 iterations)
300	IR-MRF	4.7 ± 0.02	7.3 ± 0.1	16.1 ± 0.7	191 ± 1.8
	AIR-MRF (with EIP)	3.4 ± 0.02	6.8 ± 0.1	11.9 ± 0.8	121.3 ± 0.6
	AIR-MRF (with ANN)	1.1 ± 0.02	6.7 ± 0.1	9.8 ± 0.8	107.4 ± 0.6
3000	IR-MRF	27.0 ± 0.06	73.0 ± 0.6	120.4 ± 0.7	1298.8 ± 19.2
	AIR-MRF (with EIP)	4.6 ± 0.02	32.7 ± 0.1	42.7 ± 0.9	442.1 ± 2.6
	AIR-MRF (with ANN)	1.8 ± 0.02	32.8 ± 0.1	40.5 ± 1.0	421.1 ± 3.1

we focus on the reconstruction algorithm that can provide better quality under a certain sequence design using a simplified experiment setup. We observed a non-monotonic decrease in quality with shorter sequence lengths, indicating the potential for a better sequence design. Thus future work to optimize the pulse sequence could provide additional benefits.

#### 4.4. Accelerated matching

A fast matching method is beneficial for iterative reconstruction to reduce the original prolonged dictionary matching time and compensate for the additional iterations. As shown in Table 2, with dictionary compression, both the dictionary matching and the data fidelity steps of AIR-MRF were accelerated compared to IR-MRF. The AIR-MRF reconstruction took 60% and 34% of the reconstruction time of IR-MRF. When approximate nearest neighbor search (ANN) was employed, the dictionary matching time was further decreased by a factor of approximately 3. In this study, we adopted an approximate nearest neighbor search method which has been widely used as a fast matching method [17]. The dictionary is structured as a k-dimensional tree, and each fingerprint is matched by querying the tree with an efficient binary search method to speed up matching. We also extended the current ANN method to integrate closely with the iterative reconstruction, where previous estimation information is cached to constrain the next search; this further speeds up the acquisition by increasing the search efficiency. ANN is also flexible in that the approximation level can be adjusted to balance between matching time and accuracy, which allows for an adaptive searching strategy to be integrated into the iterative reconstruction scheme in the future.

With the unbalanced SSFP pulse sequence used here, we were able to obtain adequate parameter estimates with a relative small dictionary of only ~5000 atoms; because of the computationally expensive NUFFT used for working with the spiral-sampled k-space data, the dictionary search time was a relatively small portion of overall reconstruction time. MRF setups that require larger dictionaries, such as those using balanced SSFP pulse sequences with their high sensitivity to off-resonance [29], may benefit much more from the accelerated search methods discussed here.

## 5. Conclusion

A novel MRF processing pipeline integrating iterative reconstruction with fingerprint compression, accelerated dictionary search, and regularization was demonstrated. Notable benefits of this AIR-MRF method include reduced reconstruction times and improved parameter estimate accuracy, particularly for shorter pulse sequence lengths and estimates of T2 relaxation. Future developments such as optimizing pulse sequences and spatiotemporal regularization may provide additional benefits for the proposed reconstruction pipeline.

## References

- [1] Ma D, Gulani V, Seiberlich N, Liu K, Sunshine JL, Duerk JL, et al. Magnetic resonance fingerprinting. *Nature* 2013;495:187–92. <http://dx.doi.org/10.1038/nature11971>.
- [2] Gao Y, Chen Y, Ma D, Jiang Y, Herrmann KA, Vincent JA, et al. Preclinical MR fingerprinting (MRF) at 7 T: effective quantitative imaging for rodent disease models. *NMR Biomed* 2015;28:384–94. <http://dx.doi.org/10.1002/nbm.3262>.
- [3] Chen Y, Jiang Y, Pahwa S, Ma D, Lu L, Twieg MD, et al. MR fingerprinting for rapid quantitative abdominal imaging. *Radiology* 2016;279:278–86. <http://dx.doi.org/10.1148/radiol.2016152037>.
- [4] Hamilton JL, Jiang Y, Chen Y, Ma D, Lo W-C, Griswold M, et al. MR fingerprinting for rapid quantification of myocardial T1, T2, and proton spin density. *Magn Reson Med* 2016. <http://dx.doi.org/10.1002/mrm.26216>.
- [5] Davies M, Puy G, Vanderghenst P, Wiaux Y. A compressed sensing framework for magnetic resonance fingerprinting. *SIAM J Imaging Sci* 2014;7:2623–56. <http://dx.doi.org/10.1137/130947246>.
- [6] Zhao B, Lam F, Bilgic B, Ye H, Setsompop K. Maximum likelihood reconstruction for magnetic resonance fingerprinting. *Biomed. Imaging ISBI 2015 IEEE 12th Int. Symp. on*, IEEE; 2015. p. 905–9.
- [7] Doneva M, Amthor T, Koken P, Sommer K, Börnert P. Matrix completion-based reconstruction for undersampled magnetic resonance fingerprinting data. *Magn Reson Imaging* 2017;41:41–52.
- [8] McGivney DF, Pierre E, Ma D, Jiang Y, Saybasili H, Gulani V, et al. SVD compression for magnetic resonance fingerprinting in the time domain. *IEEE Trans Med Imaging* 2014;33:2311–22. <http://dx.doi.org/10.1109/TMI.2014.2337321>.
- [9] Wang Z, Zhang Q, Yuan J, Wang X. MRF denoising with compressed sensing and adaptive filtering. *Biomed. Imaging ISBI 2014 IEEE 11th Int. Symp. on*, IEEE; 2014. p. 870–3.
- [10] Cauley SF, Setsompop K, Ma D, Jiang Y, Ye H, Adalsteinsson E, et al. Fast group matching for MR fingerprinting reconstruction. *Magn Reson Med* 2014. <http://dx.doi.org/10.1002/mrm.25439>.
- [11] Fessler JA, Sutton BP. Nonuniform fast Fourier transforms using min-max interpolation. *IEEE Trans Signal Process* 2003;51:560–74. <http://dx.doi.org/10.1109/TSP.2002.807005>.
- [12] Blumensath T. Sampling and reconstructing signals from a union of linear subspaces. *IEEE Trans Inf Theory* 2011;57:4660–71. <http://dx.doi.org/10.1109/TIT.2011.2146550>.
- [13] Blumensath T, Davies ME. Iterative thresholding for sparse approximations. *J Fourier Anal Appl* 2008;14:629–54. <http://dx.doi.org/10.1007/s00041-008-9035-z>.
- [14] Blumensath T, Davies ME. Iterative hard thresholding for compressed sensing. *Appl Comput Harmon Anal* 2009;27:265–74. <http://dx.doi.org/10.1016/j.acha.2009.04.002>.
- [15] Blumensath T, Davies ME. Normalized iterative hard thresholding: guaranteed stability and performance. *IEEE J Sel Top Signal Process* 2010;4:298–309. <http://dx.doi.org/10.1109/JSTSP.2010.2042411>.
- [16] Muja M, Lowe DG. Fast approximate nearest neighbors with automatic algorithm configuration. *VISAPP 1, 2*; 2009.
- [17] Muja M, Lowe DG. Scalable nearest neighbor algorithms for high dimensional data. *IEEE Trans Pattern Anal Mach Intell* 2014;36:2227–40. <http://dx.doi.org/10.1109/TPAMI.2014.2321376>.
- [18] Jiang Y, Ma D, Seiberlich N, Gulani V, Griswold MA. MR fingerprinting using fast imaging with steady state precession (FISP) with spiral readout. *Magn Reson Med* 2014. <http://dx.doi.org/10.1002/mrm.25559>.
- [19] Hargreaves BA. Variable-density spiral design functions. Available from: <http://mrsrl.stanford.edu/~brian/vdspiral/>; 2005.
- [20] Aubert-Broche B, Evans AC, Collins L. A new improved version of the realistic digital brain phantom. *NeuroImage* 2006;32:138–45. <http://dx.doi.org/10.1016/j.neuroimage.2006.03.052>.
- [21] High Precision Devices, Inc. Available from: <http://www.hpd-online.com/MRI-phantoms.php>; 2016.
- [22] Jiang Y, Ma D, Keenan KE, Stupic KF, Gulani V, Griswold MA. Repeatability of magnetic resonance fingerprinting T1 and T2 estimates assessed using the ISMRM/NIST MRI system phantom. *Magn Reson Med* 2016. <http://dx.doi.org/10.1002/mrm.26509>.
- [23] Uecker M, Lai P, Murphy MJ, Virtue P, Elad M, Pauly JM, et al. ESPIRiT—an eigenvalue approach to autocalibrating parallel MRI: where SENSE meets GRAPPA. *Magn Reson Med* 2014;71:990–1001. <http://dx.doi.org/10.1002/mrm.24751>.
- [24] Cline CC, Chen X, Mailhe B, Wang Q, Nadar M. AIR-MRF: accelerated iterative reconstruction for magnetic resonance fingerprinting. *Proc. Int. Soc. Magn. Reson. Med., Singapore*; 2016.
- [25] Wang Z, Li H, Zhang Q, Yuan J, Wang X. Magnetic Resonance Fingerprinting with compressed sensing and distance metric learning. *Neurocomputing* 2016;174(Part B):560–70. <http://dx.doi.org/10.1016/j.neucom.2015.09.077>.
- [26] Ma D, Coppo S, Chen Y, McGivney DF, Jiang Y, Pahwa S, et al. Slice profile and B1 corrections in 2D magnetic resonance fingerprinting. *Magn Reson Med* 2017. <http://dx.doi.org/10.1002/mrm.26580>.
- [27] Doneva M, Amthor T, Koken P, Sommer K, Börnert P. Low rank matrix completion-based reconstruction for undersampled magnetic resonance fingerprinting data. *Proc. Int. Soc. Magn. Reson. Med* 2016;0432.
- [28] Pierre EY, Ma D, Chen Y, Badve C, Griswold MA. Multiscale reconstruction for MR fingerprinting. *Magn Reson Med* 2015. <http://dx.doi.org/10.1002/mrm.25776>.
- [29] Scheffler K, Lehnhardt S. Principles and applications of balanced SSFP techniques. *Eur Radiol* 2003;13:2409–18. <http://dx.doi.org/10.1007/s00330-003-1957-x>.